Journal of Applied Physics

Liquid crystal elastomer shells with topological defect-defined actuation: Complex shape morphing, opening/closing, and unidirectional rotation

Cite as: J. Appl. Phys. **129**, 174701 (2021); https://doi.org/10.1063/5.0044920
Submitted: 20 January 2021 . Accepted: 10 April 2021 . Published Online: 03 May 2021

A. Sharma, A. M. Stoffel, and J. P. F. Lagerwall

Journal of Applied Physics ARTICLE scitation.org/journal/jap

Liquid crystal elastomer shells with topological defect-defined actuation: Complex shape morphing, opening/closing, and unidirectional rotation

Cite as: J. Appl. Phys. **129**, 174701 (2021); doi: 10.1063/5.0044920
Submitted: 20 January 2021 · Accepted: 10 April 2021 ·
Published Online: 3 May 2021

A. Sharma, A. M. Stoffel, and J. P. F. Lagerwall[a)]

AFFILIATIONS

Department of Physics and Materials Science, University of Luxembourg, 1511 Luxembourg city, Luxembourg

Note: This paper is part of the Special Topic on Programmable Liquid Crystal Elastomers.
[a)]**Author to whom correspondence should be addressed:** jan.lagerwall@lcsoftmatter.com. **URL:** http://www.lcsoftmatter.com.

ABSTRACT

We produce hollow sphere liquid crystal elastomer (LCE) actuators from a nematic precursor mixture, brought into the shape of a self-closing shell with tangential anchoring of the director field $\mathbf{n}(\mathbf{r})$, using a solvent-assisted microfluidic technique. By separating the shell production from the polymerization and cross-linking, the precursor is allowed to approach its equilibrium $\mathbf{n}(\mathbf{r})$ configuration in the shell, spontaneously forming topological defects of total strength +2. However, the photopolymerization into an LCE induces a brief but strong distortion of the overall $\mathbf{n}(\mathbf{r})$ and the defect configuration, even changing the ground state shape in the case of thick shells. The resulting LCE shells show a rich capacity for reversible shape morphing upon heating and cooling, the exact actuation mode defined by $\mathbf{n}(\mathbf{r})$, and the final defect configuration stabilized at the end of polymerization. In regions with a single +1 defect, a reversal of curvature from concave to convex is found, punctured shells exhibit a strong shape change between a nearly closed sphere at low temperature and an open-ended spherocylinder at high temperature, and all shells rotate upon actuation when suspended in a fluid. As the rotation is stronger during relaxation than during actuation, thus breaking the symmetry, the net rotation is unidirectional.

I. INTRODUCTION

The ability of liquid crystal elastomers (LCEs) to change their shape in response to heat, illumination, and other stimuli is of great practical interest, as it allows to make construction components that are their own actuators.[1,2] Because the actuation mode is determined by the relaxed-state director field $\mathbf{n}(\mathbf{r})$[3,4]—the pattern of orientational order—a powerful means of accomplishing programmed shape change is to incorporate topological defects,[5] around which $\mathbf{n}(\mathbf{r})$ is strongly modulated. This is typically done by preparing the LCE on a flat substrate with a patterned aligning layer that determines $\mathbf{n}(\mathbf{r})$,[6–13] an innovative recent addition being to emboss the target shape into an initially flat pre-LCE sheet prior to final cross-linking.[14] In all these cases, one of the states is always a flat sheet. While a few examples of LCE actuators with tubular ground state were recently presented,[15,16] $\mathbf{n}(\mathbf{r})$ was in these cases uniform, oriented along the tube long axis.

Theory suggests that the combination of curvature and topological defects in the ground state of an LCE can produce very interesting actuation behavior,[17] but so far only one corresponding experimental report exists, dealing with LCE shells produced in a microfluidic setup with in situ photopolymerization and cross-linking.[18] While the shells did provide a strong shape and internal volume change during actuation, it was difficult to correlate the actuation with the exact configuration of $\mathbf{n}(\mathbf{r})$ and the topological defects, because the very rapid process of simultaneous shell production and polymerization gave only moderate control of $\mathbf{n}(\mathbf{r})$, with a ground state that scattered light so strongly that topological defects could not be identified. The spherical shell shape is actually particularly interesting for LCEs, because the self-closing spherical topology dictates that defects with a total topological charge of +2 develop on the shell,[19,20] provided that $\mathbf{n}(\mathbf{r})$ is aligned tangentially to

the shell interfaces. Two other cases of shell-shaped LCE actuators were recently reported, one with positive[21] and one with negative[22] order parameter ground state, but in both cases the alignment was radial, hence the shells contained no topological defects.

The key to realizing spherical LCEs with well-defined topological defects is to separate shell production and polymerization stages from each other such that a tangential-aligned shell made of an LCE precursor can first adopt its equilibrium $\mathbf{n}(\mathbf{r})$ prior to initiating polymerization and cross-linking to turn the shell into an LCE. This is because the equilibrium $\mathbf{n}(\mathbf{r})$ of a tangential-aligned nematic shell can readily be tuned between configurations with two, three, or four defects by varying the thickness and asymmetry.[23–25] By switching from tangential to hybrid boundary conditions (tangential on the one side but radial on the other side) after a shell has been produced, a variety of $\mathbf{n}(\mathbf{r})$ realignment trajectories can be triggered, along which the locations, types, and number of defects change dynamically.[26,27] Moreover, if the precursor shell exhibits a nematic–smectic-A transition, the diverging elastic constants upon cooling from the nematic toward the smectic phase can be used to tune the distribution of defects;[28–30] and by photopolymerizing at the right moment, the desired configuration can be locked into place.[31] This opens an attractive route to produce intrinsically curved LCEs with actuation programmed by the topological defects developing naturally in shells, in configurations tunable by varying geometrical parameters, aligning agents, LCE precursor type, and/or temperature. Unfortunately, practical difficulties have prevented prior work from leveraging these opportunities.

These difficulties can largely be traced back to the quite different chemistry of LCE precursors compared to the *n*(O)CB-type liquid crystal molecules (mesogens) used in the vast majority of liquid crystal shell work. While *n*(O)CB mesogens provide nematic (and smectic) phases with convenient viscosity near room temperature and are easy to stabilize in shell geometry, LCE precursors are often viscous and require heating to temperature ranges where shell production becomes challenging. Even if shells are produced, their lifetime may be shorter than the time to reach an equilibrium configuration of $\mathbf{n}(\mathbf{r})$. Here, we solve these problems, first, by identifying an appropriate solvent that reduces the viscosity of the LCE precursor mixtures until shells can be produced at convenient temperatures, while also being easy to remove rapidly after production in order to bring the precursor mixture past the isotropic–nematic transition. Second, we add a small amount of an adequate member of the *n*(O)CB mesogen series, greatly increasing the shell stability beyond the time required to reach equilibrium $\mathbf{n}(\mathbf{r})$. Interestingly, we find that the final photocrosslinking step shifts the defect configuration further, yielding LCE shells with $\mathbf{n}(\mathbf{r})$ that deviates from that programmed in the precursor state. The resulting LCE shells exhibit a rich variety of reversible actuation modes with significant and complex shape morphing defined by the configuration of topological defects. When dispersed in a liquid, all shells rotate as a result of actuation and relaxation.

II. RESULTS AND DISCUSSION

A. Shell preparation

The LCE precursor mixture (details and all structures in Sec. IV) consists primarily of a mesogen with laterally affixed polymerizable side chain[32] (often referred to as "the Keller monomer") and 1,6-hexanedioldiacrylate (HDDA) as crosslinker. The precursor mixture shows a monotropic liquid crystal behavior, developing a nematic phase only on cooling from the isotropic phase ($T_{NI} \approx 80\,^{\circ}\mathrm{C}$). As shells are prepared in a three-phase coaxial capillary microfluidic setup using aqueous solutions of polyvinylalcohol (PVA) and glycerol as inner and outer phases (details in Sec. IV), the middle phase being the LCE precursor mixture which should preferably be in the isotropic state, such a high T_{NI} is challenging, further aggravated by the high viscosity of the precursor. To solve these problems, we add dioxane (boiling point 101 °C) as a water-miscible solvent that is capable of dissolving both precursor components. The miscibility with water is key, as it ensures that dioxane is rapidly removed from the LCE precursor phase into the excess of outer aqueous phase during and immediately after production, quickly bringing the shells into the nematic state.

The concentration of dioxane turns out to be very important, as too little leads to too high viscosity and sometimes even precipitation of LCE precursor components at locations of reduced temperature in the microfluidic setup, and too much yields a mixture that wets the capillary walls, preventing shell formation, and it may even lead to complete dissolution of the shells. Table I summarizes our experiments for finding the optimal composition, which we identified at 15 wt. % dioxane. This leads to successful production of shells without significant wetting, as shown in Fig. 1. Dioxane is removed so rapidly that the transition to nematic phase takes place already during shell production, the shells being stably nematic as they are collected in a vial at the end of the microfluidic setup.

After production, the shells need to be annealed above 65 °C in order to avoid crystallization, until surplus topological defects and random deformations have healed out, $\mathbf{n}(\mathbf{r})$ approaching its equilibrium configuration. Because the mixture is quite viscous, it can take hours to reach this state. Unfortunately, shells of the pure LCE precursor mixture collapse within seconds to minutes after collection, despite the stabilizing effect of the PVA in the surrounding aqueous phases. Inspired by the well-known stability of shells made from *n*(O)CB mesogens in aqueous PVA solutions, we solve this problem by adding 1 mol. % of 7OCB, chosen due to its

TABLE I. Observations from microfluidic shell production with varying concentrations of dioxane mixed to the LCE precursor.

Dioxane (wt. %)	LCE precursor (wt. %)	Result
40	60	Complete intermixing of LCE and aqueous phases
30	70	Mere droplet formation due to partial intermixing
20	80	Successful shell production but wetting issues in the microfluidic device
15	85	Successful shell production without major wetting issues
10	90	LCE precursor not completely dissolved in dioxane

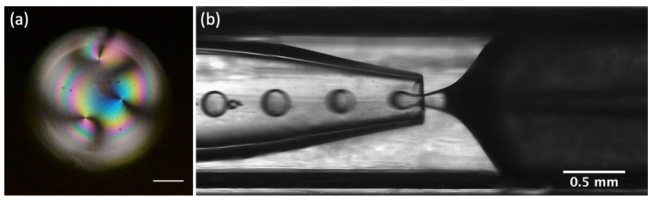

FIG. 1. Image (a) is a polarizing optical microscopy (POM) image of a shell with equilibrium configuration of **n**(**r**), exhibiting three +1/2 defects near the thinnest point of the shell (the top; in focus), the fourth near the equator. Scale bar represents 100 μm. Image (b) shows a still frame from the microfluidic production of shells.

nematic phase having a similar temperature range to that of the LCE precursor. This small amount of 7OCB does not significantly influence the temperature range of nematic phase of the LCE precursor mixture but it greatly improves the shell stability, giving shells a lifetime more than enough to allow the required annealing.

B. Polymerization of shells

The time for shells to achieve a configuration suitable for polymerization depends on their thickness. We generally do not wait until the equilibrium configuration has been reached but initiate polymerization once an interesting well-defined configuration of **n**(**r**) is identified, which typically takes around 20–25 min. The most common configuration has four +1/2 defects near the thinnest point of the shell [Figs. 2(a) and 2(b); Multimedia view] but sometimes a configuration closer to the tetrahedral arrangement of four +1/2 defects is seen [Fig. 2(d); Multimedia view]. Thicker shells often remain with a poorly defined director field as in Fig. 2(c) (Multimedia view). In very rare cases, a well-defined **n**(**r**) configuration with more than the minimum required defects, i.e., with positive- as well as negative-valued defects, can be found. An example is shown in Fig. 2(e) (Multimedia view), where two +1 and one +1/2 defects can be seen between the equator and top of the shell, by topological necessity requiring at least one −1/2 defect to reside on the bottom shell side, most likely more.

In our basic procedure, a photoinitiator (PI) is included in the LCE precursor mixture, allowing polymerization of the precursor shells into an LCE to be initiated by UV-light irradiation. Additionally, we explore the preparation of shells without PI in the precursor mixture, adding instead a reasonably water-soluble PI to the inner as well as outer aqueous phases. Both approaches work. The former has the disadvantage that some PI tends to leak out from the shell into the aqueous phases during production, making it difficult to control the amount of PI at the polymerization stage. The latter allows better control but requires a much larger PI concentration, given the greater volume of the outer aqueous phase. While the exact process of initiation for the case of water-dissolved PI needs to be investigated in more detail, we speculate that some fraction of the unexposed PI may diffuse from the aqueous phases into the precursor shell, initiating polymerization from within the shell upon UV exposure. Alternatively, free radicals from UV-exposed PI in the aqueous phase in the close vicinity to a shell may diffuse close enough to the interface to react with an exterior monomer, the addition reaction then propagating within the shell. We have started a systematic investigation of this issue and will publish the results elsewhere.

As the microfluidic production method yields hundreds of shells within about a minute, it is difficult to keep track of individual shells throughout the process from shell production, via polymerization, to actuation. However, we film several shells with representative director fields during the polymerization process to understand how the texture changes as a result of polymerization. As can be seen in Fig. 2 (Multimedia view), the photopolymerization dramatically changes the director field. It appears as if the polymerization induces a brief but strong expansive flow along the local **n**(**r**), and a corresponding compressive flow in the perpendicular direction, leading to the defects moving around on the spherical shell during the process, see, e.g., the trajectories of defects in Fig. 2(a) (Multimedia view) and of dark inclusions in Fig. 2(c) (Multimedia view). Considering that these textural changes occur while the shells transform from a low molar mass liquid to an elastomeric state, it is difficult to assess if the phenomenon reflects mainly an actual material flow (possibly involving diffusion driven by concentration gradients resulting from spatial variations in the rate of the polymerization reaction), a straining of the elastomer as it is forming, or both. In strongly asymmetric shells, such as in sequences (a) and (b), the motion seems to be driven mainly by the back side of the shell, with more uniform initial **n**(**r**). This is reasonable as the back side is considerably thicker than the front side, which contains the defects. Sometimes different defects move in different directions [Figs. 2(a) and 2(d); Multimedia view], sometimes all defects move as a cluster [Fig. 2(b); Multimedia view].

Thin shells generally appear to retain their spherical shape but this is not the case for thick shells, which can undergo significant shape deformation as a result of the polymerization, see Figs. 2(c) and 2(d) (Multimedia view). The shape change can also shift the center of gravity, inducing a rotation of the shell over the course of a minute, as seen in Fig. 2(d) (Multimedia view). We recently observed similar strong shape changes, with a significant bulging-out around the thinnest point of the shell, when polymerizing non-elastomeric cholesteric liquid crystal shells.[33] We argue that the origin is the frustration caused by the polymerization-induced shrinkage of acrylate mesogens[34]—used in our previous study[33] as well as in the present work—in a self-closing spherical shell that fully envelops an incompressible inner fluid droplet: since the inner droplet volume remains unchanged, the shrinking shell must distort from the spherical shape to keep accommodating the enclosed liquid. It undergoes different amounts of strain in different parts of the shell, due to the thickness variations[33] and, in this case, also probably due to the local variations in uniformity in **n**(**r**) and the presence of defects.

While **n**(**r**) generally loses some of its high definition during the polymerization process, it is still possible to identify topological defects and estimate the main features of **n**(**r**) in the resulting LCE shells if they are thin, as in Figs. 2(a) and 2(b) (Multimedia view). For thicker shells, the analysis is more challenging, but here we are helped by a third consequence of the photopolymerization process: once the motion has stopped and the final LCE state is stable, we notice that a regular pattern of parallel thin stripes has often

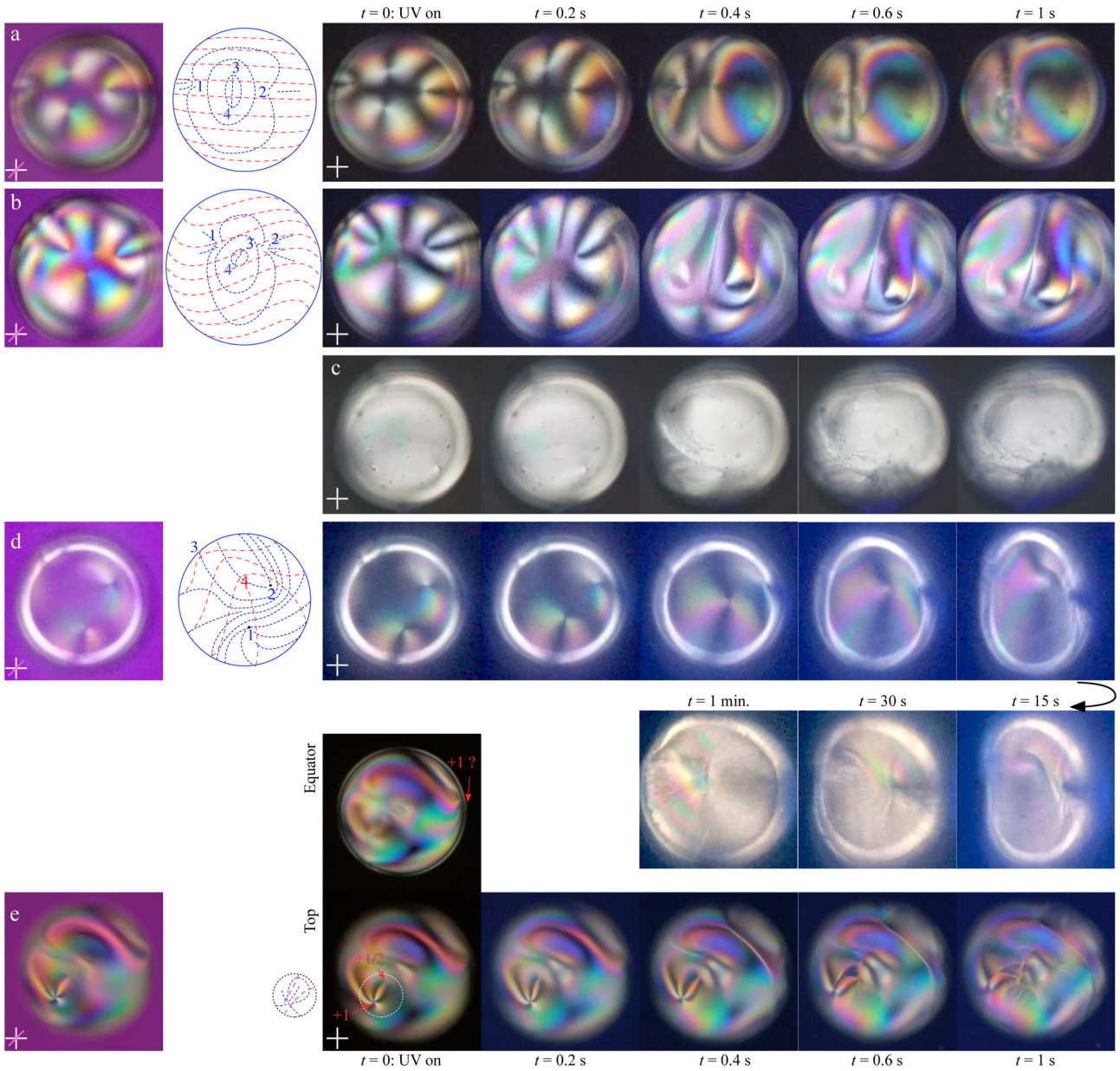

FIG. 2. Shell reconfiguration during polymerization at 65 °C monitored in POM, initiated 20–30 min after shell production. Sequences (a) and (b) show highly asymmetric shells where all four +1/2 defects are collected near the thinnest point, at the top of the shell (in focus), but with slightly different starting configurations. Sequence (c) shows a shell that is so thick that **n**(**r**) cannot be mapped out, as the entire shell scatters light and appears equally bright irrespective of shell orientation. Sequence (d) shows a shell with an initial **n**(**r**) that approaches a tetrahedral defect configuration, with one defect on the back side of the shell and one at the edge (the former is not seen with this focus, the latter is seen as a black line across the rim). The leftmost column in (a), (b), (d), and (e) shows POM images of each shell with a first-order λ-plate inserted. Based on these images, the corresponding starting **n**(**r**) are estimated as sketched in the second column. The red long-dashed lines indicate **n**(**r**) on the back side and the blue short-dashed lines **n**(**r**) on the front side (in focus). Sequence (e) shows a shell in which surplus defects had not yet annealed, hence we can identify +1 and +1/2 defects in direct vicinity near the shell top, and another +1 defect appears to reside at the equator. On the back side, negative-signed defects must be present to meet topological constraints. We sketch the director field only within a small region for this complex configuration. Sequences (a)–(c) are obtained with the photoinitiator added in the LCE precursor, whereas for (d) and (e) it was added into the aqueous phases (inner as well as outer). The shell diameter prior to polymerization is (a) 170 μm; (b) 321 μm; (c) 340 μm; (d) 235 μm; and (e) 265 μm. Multimedia views: https://doi.org/10.1063/5.0044920.1; https://doi.org/10.1063/5.0044920.2; https://doi.org/10.1063/5.0044920.3; https://doi.org/10.1063/5.0044920.4; https://doi.org/10.1063/5.0044920.5

developed in thick shells. While we have not studied their origin in detail, it appears that the stripes orient perpendicular to the original $\mathbf{n}(\mathbf{r})$, see, e.g., video frame 1 s after UV irradiation in Fig. 2(d) (Multimedia view). Here, horizontal stripes can be seen toward the bottom of the image, where the director field was originally vertical (as can be seen by following the process from the initial $\mathbf{n}(\mathbf{r})$, sketched in the second column). Thanks to these stripes, we can make rough assessments of how $\mathbf{n}(\mathbf{r})$ is oriented in thick shells, even if the details are difficult to determine.

Such stripe formation perpendicular to the original $\mathbf{n}(\mathbf{r})$ has been observed under strain perpendicular to $\mathbf{n}(\mathbf{r})$ in polysiloxane[35] and polyacrylate LCEs,[36] attributed to a "soft elasticity"-mediated rotation of $\mathbf{n}(\mathbf{r})$ in opposite directions in adjacent stripes.[34,37] We tentatively propose that the same phenomenon is at the origin of the stripes seen in the shells, as they experience an effective tensile stress due to the resistance of the inner incompressible fluid against the polymerization-induced shrinkage as the LCE is being formed. Ignoring the thickness variations, the spherical symmetry should make the tensile stress isotropic in the plane of the shell, and in shells that are thin and exhibit an originally radial $\mathbf{n}(\mathbf{r})$ also the strain ends up being isotropic in the shell plane.[22] In this case, however, the considerable thickness variations and the tangential $\mathbf{n}(\mathbf{r})$ break the spherical symmetry, yielding strains that vary in intensity and direction throughout the shell, as seen in the considerable shape changes discussed above. As the elastomeric network is intrinsically stretched out along $\mathbf{n}(\mathbf{r})$ as it is formed,[3] it should be easier for it to respond to the in-plane-isotropic stress by straining mainly perpendicular to $\mathbf{n}(\mathbf{r})$, in alternating directions, thus giving rise to the stripes.

C. Actuation upon temperature variation

In order to study the actuation and relaxation behavior of the LCE shells, we place polymerized shells on a glass slide together with some of the outer aqueous phase (which contains 50% glycerol, allowing it to be heated to the ∼135 °C required for complete actuation) in order to observe the shell's motion while suspended in liquid. For reference, we also remove the outer aqueous phase from some shells, either by blotting with a tissue paper or by washing with excess acetone, which is then evaporated. While this in principle allows the study of actuation in air, we will see below that the glass substrate on which the shell is supported strongly reduces the ability to actuate. Depending on the ground state shape and $\mathbf{n}(\mathbf{r})$ of an LCE shell, quite different actuation modes arise. We here select four representative shells, displaying three characteristic actuation modes, discussing each mode in turn. All four shells were polymerized using a photoinitiator added to the aqueous phases.

Note that LCEs never go entirely isotropic upon heating, due to the cross-linked polymer network retaining some order. Nevertheless, a beneficial aspect of LCEs based on the Keller monomer is that a practical T_{NI} can still be defined, as the residual orientational order is small, resulting in a very significant reduction in birefringence. For the polymerized LCE, we find $T_{NI} \approx 120\,^{\circ}\mathrm{C}$, with the main actuation window being in the approximate range 115–120 °C. The relaxation window, on cooling, appears to be about 5 °C lower, but this may be partially an artifact due to the inertia in cooling the shell as it is suspended in a liquid which first has to be cooled itself. Unfortunately, the distortion of $\mathbf{n}(\mathbf{r})$ during polymerization is often so strong that we do not feel confident to draw the ground state director field. With future refinements of the polymerization procedure, we hope to be able to correlate the observed actuation to $\mathbf{n}(\mathbf{r})$ in the ground state with accuracy.

1. Actuation of closed shells: Shape change and rotation

Figure 3 (Multimedia view) shows a closed shell with largely concentric $\mathbf{n}(\mathbf{r})$ in the ground state, as imaged in the first panel in (a), where one topological defect can also be located to a point on the equator. Its character cannot be clearly identified, however. As we heat the shell toward T_{NI} of the LCE, we see a strong rotation of the internal texture, which translates in a physical rotation of the actual shell, as seen by tracing the location of the topological defect, highlighted by a green arrow in Fig. 3(a) (Multimedia view). The ground state director field initially in focus (a, 97 °) is dominated by a large crescent-like section with concentric $\mathbf{n}(\mathbf{r})$, as indicated by the radial stripe pattern. On heating through the actuation temperature window (about 110–121 °C), the LCE contracts along $\mathbf{n}(\mathbf{r})$ and expands in the perpendicular direction, resulting in an internal rotational motion in parallel with a shrinkage of the cross section seen in POM. The actuation also leads to a shape change, the full 3D character of which we cannot elucidate from the POM images, but we note that the cross section turns somewhat elliptical and has a reduced area. Since the core of the shell contains an incompressible liquid and the shell is closed, the internal volume must be nearly constant (ignoring the thermal expansion within

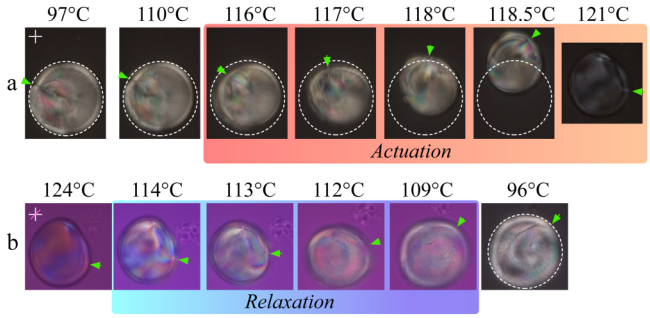

FIG. 3. POM images of actuation on heating (a) and relaxation on cooling (b) of a closed relatively thick shell. One topological defect is seen in the ground state, highlighted with a green arrow throughout the process. A second defect can be seen at high temperature, best in (b) at 124 °C. The shape change during actuation leads to a macroscopic rotation as well as translation of the shell, as highlighted by the dashed circle which has the diameter and location of the ground state shell in all images. Above 118.5 °C, the shell moves out of the POM image frame and the stage thus had to be translated to follow the shell, hence the image at 121 °C no longer reflects the location of the shell. During cooling, a first-order λ-plate has been inserted in the POM. Note also that a small dust particle has attached to the shell, which rotates with it. The ground state shell diameter is 280 μm. All temperature values correspond to the hot-stage readout, which is not the true temperature in the shell, due to the inertia given by the need to heat or cool the liquid in which the shell resides. Temperature differences are reliable, however. Multimedia view: https://doi.org/10.1063/5.0044920.6

the relatively small temperature window of actuation), i.e., the shell must expand in the vertical dimension, along the viewing direction in the experiment.

On cooling, the shell relaxes almost to its initial state, retaining its original cross section size and a shape very near circular, and in the process it rotates in the opposite sense compared to the rotation during actuation. Interestingly, during this experiment, a small dust particle attached to the shell toward the end of the actuation process. It is made easier to see by the introduction of a first-order λ-plate in Fig. 3(b) (Multimedia view). This becomes a

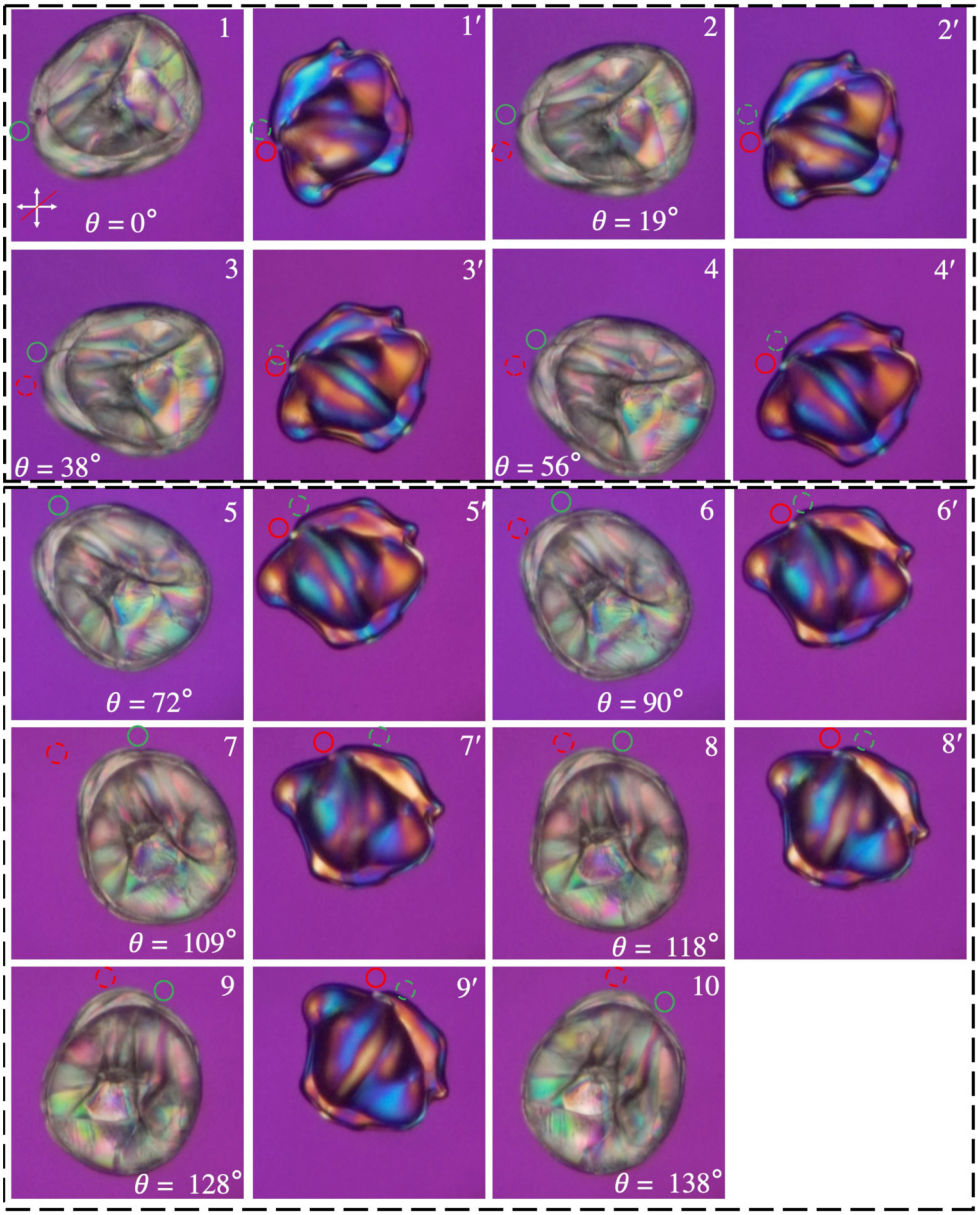

FIG. 4. Unidirectional rotation of a shell across multiple heating–cooling cycles. The shell in the ground state is shown with unprimed numbers, the numbers counting the heating-cooling cycles. The corresponding high-temperature images (after completed shape morphing) are shown with primed numbers. Solid green and red circles show a selected reference point on the shell in the ground and actuated state, respectively. Dashed green and red circles show the position of this reference point in the previous frame, to highlight the rotation. The angle θ represents the net rotation (measured in the ground state) with respect to image 1, where we define $\theta = 0°$. Because of the movement of the shell during the experiment, the microscope stage had to be translated, thus after image 4', the image frame position with respect to the lab frame was changed. It remains unchanged in images 5–10. Multimedia view: https://doi.org/10.1063/5.0044920.7

"cargo" that the shell brings with it in its rotation, clearly demonstrating that the rotation we see is a physical rotation of the actual material, not just a reorientation of the internal texture.

In order to investigate the rotation of LCE shells in liquid more systematically, we study the repeated actuation and relaxation of another shell, heating and cooling it through the transition window ten times consecutively to analyze the net rotation. In Fig. 4 (Multimedia view), we show POM images as obtained with an inserted first-order λ plate, in the ground state (unprimed numbers) and in the actuated state (primed numbers), above T_{NI}. We see that every time we cool the shell from the actuated state it rotates a significant amount clockwise, while on heating the rotation is anticlockwise but somewhat smaller in magnitude. The net effect of a full cycle is thus a clockwise rotation. While the strong change in shape as well as in birefringence makes it difficult to measure the exact rotation during a single actuation or relaxation, respectively, it is quite straightforward to measure the rotation angle between two consecutive low- or high-temperature states, respectively, as indicated in the figure. Some uncontrolled convection in the continuous phase as well as rotations out of plane complicate the measurement, yielding variations between cycles in the apparent in-plane rotation angle, but we can conclude that the average net clockwise rotation is about 15° per cycle.

The magnitude and sense of rotation changes from shell to shell, depending upon the original shape, defect configuration, radius, and thickness. Future studies need to apply additional imaging methods to capture the full 3D rotation and correlate it to the starting configuration, but we can at this stage conclude that a net unidirectional rotation of shells suspended in a liquid is commonly observed. Considering that the microfluidic production method allows a large number of LCE shells to be produced with a quite high throughput, this rotation might be put to use, e.g., in microfluidic setups that are independent of external pumps for creating a rotational flow. If each shell is attached at one point to a pillar, the rotation might also be utilized for closing and opening channels, although for such an application a configuration needs to be identified that reliably gives the bidirectional rotation of constant magnitude on actuation and relaxation, respectively.

2. Actuation of punctured shell: Opening and closing with significant shape morphing

In the next experiments, we study the actuation of a shell that has been punctured at one point. We first actuate it in the aqueous liquid phase and then in air. As shown in Figs. 5(a)–5(c)

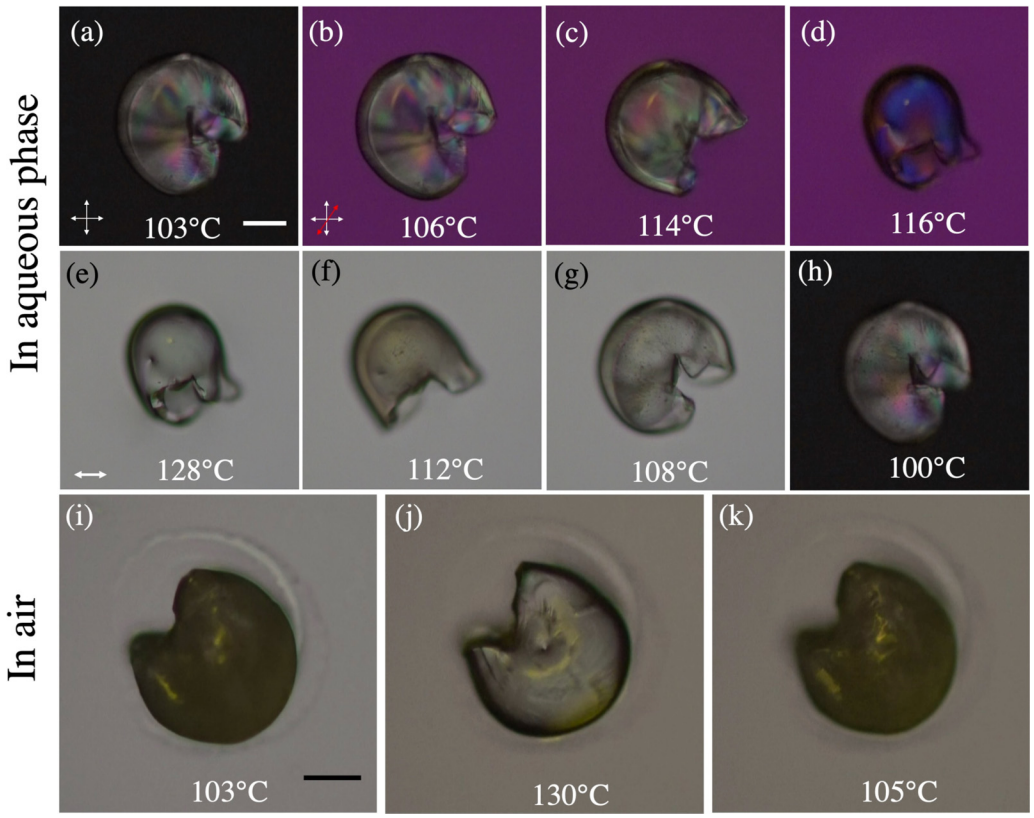

FIG. 5. POM images of heating-induced actuation and cooling-induced relaxation of a broken shell. Images (a)–(h) show the shape morphing as a function of temperature when the shell is in the aqueous phase. Images (i)–(k) show the same shell at low and high temperature in the absence of the aqueous phase. Scale bars represent 50 μm. Multimedia views: https://doi.org/10.1063/5.0044920.8; https://doi.org/10.1063/5.0044920.9

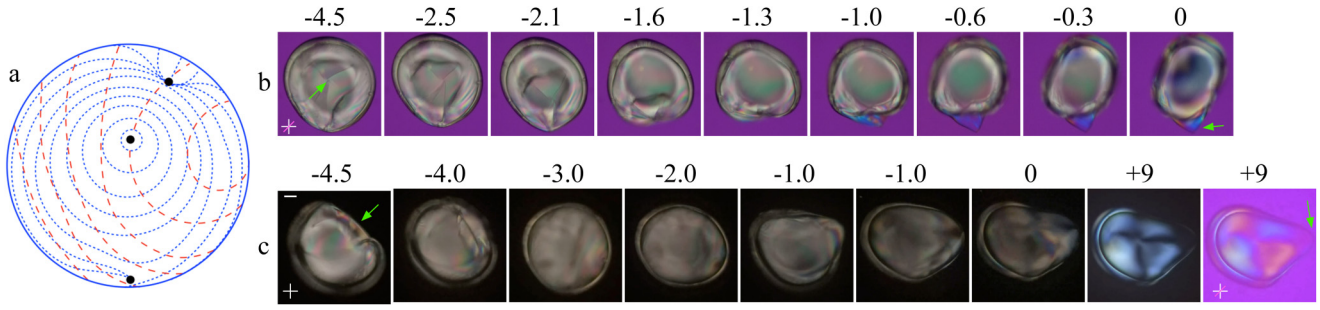

FIG. 6. POM images of the actuation of an LCE shell with a +1 defect on the thinner side, an estimated **n**(**r**) sketched in (a), using the same graphical coding as in Fig. 2. In (b), the shell is imaged from the top and in (c) it is imaged from the side in the ground state. During heating, the initially concave indentation around the defect inverts into a convex protrusion. The numbers above each image indicate the relative temperature difference (in °C) compared to the temperature of completed actuation. Scale bar represents 50 μm. Multimedia views: https://doi.org/10.1063/5.0044920.10; https://doi.org/10.1063/5.0044920.11

(Multimedia view), the shell has an apparent nearly spherical ground state shape below T_{NI}, with a small opening visible at the bottom right. On heating to the actuation temperature range, the shell rotates, as for closed shells, and shrinks quite significantly in size, see Figs. 5(d) and 5(e) (Multimedia view). Note that there is no longer any constraint of constant volume, as the liquid inside can easily flow in or out. The opening becomes much larger on heating, leaving the shell with an open-ended spherocylinder shape. During actuation, we note that the upper jaw around the opening remains largely in place, while the lower jaw rotates significantly, leading to the increased opening size. On cooling back to the nematic state, the LCE relaxes reversibly, reducing the size of the opening again until the shell has recovered the original nearly closed spherical ground state shape. This type of actuation might be of interest for controlled substance release (actuate to open), as well as for sampling from liquid environments (relax to close).

We now remove the surrounding aqueous phase from this shell in order to study its actuation while lying on a glass substrate and otherwise surrounded by air, as shown in Figs. 5(i)–5(k) (Multimedia view). We note that the birefringence appears different in air compared to in the aqueous phase, possibly related to the different angle of light refraction at the shell boundaries, changing the optical path length as well as the path orientation with respect to the local optic axis. On heating, we no longer see any significant actuation, the sole response being a greater transparency. We believe it is the adherence of the shell to the glass substrate that prevents it from actuating, indicating that the LCE shell actuators work best when suspended in liquid phases. Possibly, a coating with anti-adherent powder like corn starch, as is frequently used to avoid stickiness also from regular elastomers, might reduce the impact from the solid interface.

3. Actuation of closed shell with isolated +1 defect: Strong shape morphing with curvature inversion

While most shells exhibit solely +1/2 defects, some shells show one or more +1 defects. A particularly interesting example is the LCE shell in Fig. 6 (Multimedia view), which exhibits a quite well isolated +1 defect at the thinner side. We study actuation and relaxation (only actuation is shown in the figure but both directions are shown in the videos) of this shell, viewing it from two different sides at the onset. In Fig. 6(b) (Multimedia view), the +1 defect starts out at the top of the shell, in the middle of the cross section as we view it in the POM (highlighted by a green arrow), while in (c) it is in the plane of the cross section, at the upper right corner of the image. The latter view shows that the ground state shell buckles inwards at the location of the defect, giving it a concave shape at this point.

As we heat the shell (the numbers on top show the temperature offset in °C with respect to the temperature of completed actuation) through the actuation temperature window, it undergoes a complex shape morphing coupled to a rotation, but we clearly see in both views that the shell inverts its curvature around the defect, switching from concave at low temperature to convex at high temperature. The high-temperature images show a quite marked protrusion at the defect, highly reminiscent of the theoretical prediction for actuation around a concentric +1 defect by Modes and Warner.[17] Indeed, by analyzing the POM image with inserted first-order λ-plate at 9 °C above the temperature of completed shape morphing in Fig. 6(c) (Multimedia view), we see that **n**(**r**) is concentric around the protrusion.

III. CONCLUSIONS AND OUTLOOK

We have for the first time been able to produce tangential-aligned hollow shells of liquid crystal elastomer (LCE) precursor without simultaneous polymerization and cross-linking, with sufficient lifetime to allow annealing of the director field into its equilibrium configuration, or other interesting well-defined configurations, while the shell remains in a low molar mass state. Surprisingly, we find a strong deformation of **n**(**r**) during the subsequent photopolymerization and cross-linking. The main breakthrough of this paper is the ability to separate shell production and polymerization, thus opening a new door to tailoring director fields, with topological defects naturally included, in intrinsically curved LCEs. While we could also demonstrate a variety of interesting novel actuation modes, future work needs to fine-tune the

details—in particular, regarding the photopolymerization step in order to minimize the related director field distortion—and employ 3D imaging techniques to fully elucidate the relationship between the complex shape morphing, rotation, and translation behavior of the shells, and their ground state director field configurations, as programmed during cross-linking.

When specific modes of actuation can be reliably produced, possibly using modified LCE chemistries for lower actuation temperature window, new applications may be envisaged, for instance, in closed-loop microfluidic setups requiring no external pumps, or drug release to or sampling from biological fluids. To this end, alternative means for triggering the actuation need to be incorporated, e.g., by including UV-sensitive dyes that disturb the order upon photoisomerization, allowing actuation by light, or by including nanoparticles that absorb the energy from suitable radiation, allowing the LCE alone to be heated to the actuation window without changing the temperature of the surrounding fluid.

IV. MATERIALS AND METHODS

The structures of all chemicals used are shown in Fig. 7. We prepare the LCE precursor by adding 10 mol. % of 1,6-hexanediol diacrylate as crosslinker to the reactive mesogen 4-acryloyloxybutyl 2,5-(4-butyloxybenzoyloxy)benzoate ("Keller monomer"). For making shells with photoinitiator (PI) in the LCE phase, we add 0.5 mol. % PI benzoin methyl ether (BME) in the mixture. We also add 1 wt. % 4-Cyano-4'-n-heptyloxybiphenyl (7OCB) LC as additional stabilizer and 15 wt. % dioxane as solvent in the mixture. The mixture is stirred at 80 °C for 7–8 h inside a vial covered by aluminum foil to protect against light exposure, as this would otherwise initiate polymerization prematurely. Throughout all further steps of the shell preparation, annealing, and investigation prior to polymerization into an LCE, all work is done in a lab equipped with yellow light for the same reason.

For the aqueous phase, we first prepare a solution of 10 wt. % weakly hydrolyzed (87%–89%) polyvinylalcohol (PVA) with low molar mass (13–23 kg/mol) by stirring at 70–80 °C for 2 days. This PVA solution is mixed with glycerol at 50:50 volume ratio to form the isotropic liquid flowed as inner and outer aqueous phases during the shell production. In the case when we polymerize shells by adding PI in the aqueous phase, we add 5 wt. % of the water-soluble PI 2-Hydroxy-4-(2-hydroxyethoxy)-2-methylpropiophenone in this mixture of glycerol and PVA–water solution.

To prepare shells, we follow the nested capillary microfluidic method developed by Weitz and co-workers.[38] The inner aqueous phase is flowed through a tapered cylindrical capillary (inlet) with 70 μm diameter orifice, the LCE precursor mixture flowing in the same direction in the interstitial space between the inlet and a square capillary in which the inlet is inserted, with inner side length equal to the inlet outer diameter. The LCE precursor phase and the inner aqueous phase are flow-focused by the outer aqueous phase, which is flowing in the opposite direction in the interstitial space between the same square capillary and a second tapered cylindrical capillary (orifice size of 350 μm) functioning as outlet, oriented opposite of the inlet. The resulting shells exit through the outlet capillary, which is connected to soft tubing ending in another vial filled with the aqueous phase mixture kept at 65–70 °C, in which the shell suspension is collected.

In order to maintain all fluids at an appropriate temperature for shell production, we fill them into glass vials which are placed in a heating block kept at 80 °C. To avoid significant temperature drops during passage through tubing from the vial to the nested capillary device, we irradiate the tubing with an IR lamp. The nested capillary device itself is mounted on a Linkam hot stage (T96-p) kept at 80 °C, and this setup is placed on an inverted microscope (Nikon, Eclipse TS100) equipped with a high-speed camera (IDT NX4-S3). The flow rate of each fluid is adjusted by a pneumatic flow control unit (Fluigent MFCS-EZ), which pressurizes each vial to induce a flow at the desired rate.

After production, the shells remain in the collection vial for 20–30 min, at a temperature of 65–70 °C, in order to allow annealing of the director field toward an equilibrium configuration. We

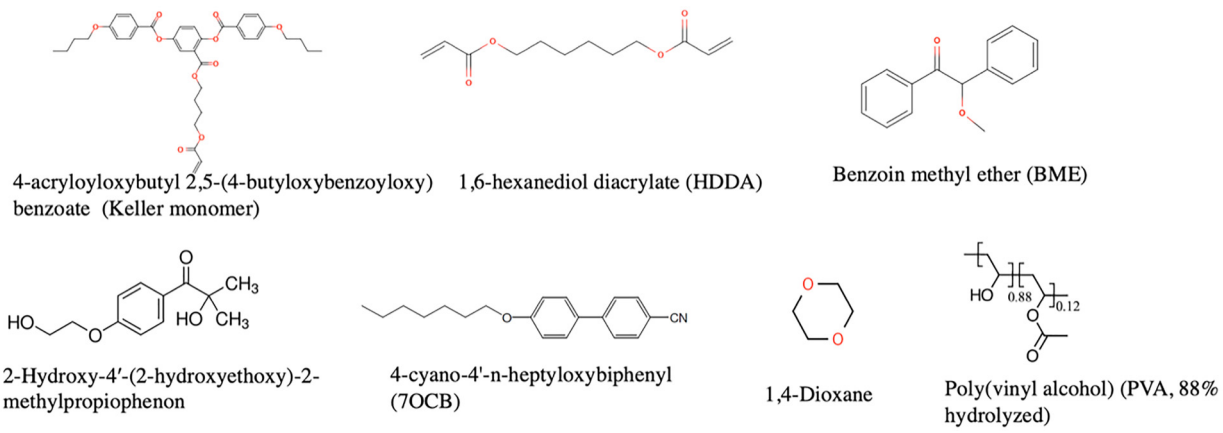

FIG. 7. Chemical structures of reactive mesogen ("Keller monomer"), cross linker (HDDA), LCE-soluble photoinitiator (BME), water-soluble photoinitiator, stabilizing nematic LC (7OCB), water-miscible LCE solvent (dioxane), and polymeric stabilizer (PVA).

generally start photopolymerization well before the equilibrium state has been reached, by shining UV light onto the shells, using a UVATA LED UV curing system (8800 mW cm^{-2} at full power, 365 nm wavelength) for 3 min. After photopolymerization, we take a few shells out on a glass slide for observation in a polarizing microscope (ECLIPSE LV100ND) equipped with a video camera (Sony camcorder, FDR-AXP 33). When we take shells out, we also take some aqueous phase with them. Since this contains glycerol, it does not evaporate for a long time. We keep this glass slide inside a Linkam hot stage (THMS600) mounted on the microscope in order to study the actuation and relaxation as a function of temperature.

ACKNOWLEDGMENTS

We thank M. Magrini and R. Kizhakidathazhath for helpful discussions concerning chemistry-related issues. The authors acknowledge the financial support from the European Research Council under the European Union's H2020 Programme/ERC Grant Agreement No. 648763 (consolidator project INTERACT). A. Sharma acknowledges financial support from the Fonds National de la Recherche (FNR, doctoral training grant PRIDE MASSENA, grant code 2016/10935404).

DATA AVAILABILITY

The data that support the findings of this study are available from the corresponding author upon reasonable request.

REFERENCES

[1]J. M. McCracken, B. R. Donovan, and T. J. White, "Materials as machines," Adv. Mater. **32**, 1906564 (2020).
[2]T. White and D. Broer, "Programmable and adaptive mechanics with liquid crystal polymer networks and elastomers," Nat. Mater. **14**, 1087–1098 (2015).
[3]M. Warner and E. M. Terentjev, *Liquid Crystal Elastomers* (Oxford University Press, 2007), p. 424.
[4]E. Fleischmann and R. Zentel, "Liquid-crystalline ordering as a concept in materials science: From semiconductors to stimuli-responsive devices," Angew. Chem. Int. Ed. **52**, 8810–8827 (2013).
[5]C. D. Modes and M. Warner, "Blueprinting nematic glass: Systematically constructing and combining active points of curvature for emergent morphology," Phys. Rev. E **84**, 021711 (2011).
[6]H. Kim, J. A. Lee, C. P. Ambulo, H. B. Lee, S. H. Kim, V. V. Naik, C. S. Haines, A. E. Aliev, R. Ovalle-Robles, R. H. Baughman, and T. H. Ware, "Intelligently actuating liquid crystal elastomer-carbon nanotube composites," Adv. Funct. Mater. **29**, 1905063 (2019).
[7]G. Babakhanova, T. Turiv, Y. Guo, M. Hendrikx, Q.-H. Wei, A. P. H. J. Schenning, D. J. Broer, and O. D. Lavrentovich, "Liquid crystal elastomer coatings with programmed response of surface profile," Nat. Commun. **9**, 1087 (2018).
[8]T. Guin, M. Settle, B. Kowalski, A. Auguste, R. Beblo, G. Reich, and T. White, "Layered liquid crystal elastomer actuators," Nat. Commun. **9**, 2531 (2018).
[9]T. Ware, M. McConney, J. Wie, V. Tondiglia, and T. White, "Actuating materials. Voxelated liquid crystal elastomers," Science **347**, 982–984 (2015).
[10]S. Iamsaard, S. Aßhoff, B. Matt, T. Kudernac, J. Cornelissen, S. Fletcher, and N. Katsonis, "Conversion of light into macroscopic helical motion," Nat. Chem. **6**, 229–235 (2014).
[11]L. T. de Haan, V. Gimenez-Pinto, A. Konya, T.-S. Nguyen, J. M. N. Verjans, C. Sánchez-Somolinos, J. V. Selinger, R. L. B. Selinger, D. J. Broer, and A. P. H. J. Schenning, "Accordion-like actuators of multiple 3D patterned liquid crystal polymer films," Adv. Funct. Mater. **24**, 1251–1258 (2014).
[12]M. McConney, A. Martinez, V. Tondiglia, K. Lee, D. Langley, I. Smalyukh, and T. White, "Topography from topology: Photoinduced surface features generated in liquid crystal polymer networks," Adv. Mater. **25**, 5880–5885 (2013).
[13]L. de Haan, C. Sánchez-Somolinos, C. Bastiaansen, A. Schenning, and D. Broer, "Engineering of complex order and the macroscopic deformation of liquid crystal polymer networks," Angew. Chem. Int. Ed. **51**, 12469–12472 (2012).
[14]M. Barnes and R. Verduzco, "Direct shape programming of liquid crystal elastomers," Soft Matter **15**, 870–879 (2019).
[15]Q. He, Z. Wang, Y. Wang, A. Minori, M. Tolley, and S. Cai, "Electrically controlled liquid crystal elastomer-based soft tubular actuator with multimodal actuation," Sci. Adv. **5**, eaax5746 (2019).
[16]L. B. Braun, T. Hessberger, E. Pütz, C. Müller, F. Giesselmann, C. A. Serra, and R. Zentel, "Actuating thermo- and photo-responsive tubes from liquid crystalline elastomers," J. Mater. Chem. C **6**, 9093–9101 (2018).
[17]C. D. Modes and M. Warner, "Responsive nematic solid shells: Topology, compatibility, and shape," EPL **97**, 36007 (2012).
[18]E.-K. Fleischmann, H.-L. Liang, N. Kapernaum, F. Giesselmann, J. P. F. Lagerwall, and R. Zentel, "One-piece micropumps from liquid crystalline core-shell particles," Nat. Commun. **3**, 1178 (2012).
[19]M. Urbanski, C. G. Reyes, J. Noh, A. Sharma, Y. Geng, V. S. R. Jampani, and J. P. Lagerwall, "Liquid crystals in micron-scale droplets, shells and fibers," J. Phys.: Condens. Matter **29**, 133003 (2017).
[20]T. Lopez-Leon and A. Fernandez-Nieves, "Drops and shells of liquid crystal," Colloid Polym. Sci. **289**, 345–359 (2011).
[21]V. S. R. Jampani, D. J. Mulder, K. R. De Sousa, A.-H. Gélébart, J. P. F. Lagerwall, and A. P. H. J. Schenning, "Micrometer-scale porous buckling shell actuators based on liquid crystal networks," Adv. Funct. Mater. **28**, 1801209 (2018).
[22]V. S. R. Jampani, R. H. Volpe, K. Reguengo de Sousa, J. Ferreira Machado, C. M. Yakacki, and J. P. F. Lagerwall, "Liquid crystal elastomer shell actuators with negative order parameter," Sci. Adv. **5**, eaaw2476 (2019).
[23]V. Koning, T. Lopez-Leon, A. Darmon, A. Fernandez-Nieves, and V. Vitelli, "Spherical nematic shells with a threefold valence," Phys. Rev. E **94**, 012703 (2016).
[24]V. Koning, T. Lopez-Leon, A. Fernandez-Nieves, and V. Vitelli, "Bivalent defect configurations in inhomogeneous nematic shells," Soft Matter **9**, 4993–5003 (2013).
[25]T. Lopez-Leon, V. Koning, K. B. S. Devaiah, V. Vitelli, and A. Fernandez-Nieves, "Frustrated nematic order in spherical geometries," Nat. Phys. **7**, 391–394 (2011).
[26]G. Durey, Y. Ishii, and T. Lopez-Leon, "Temperature-driven anchoring transitions at liquid crystal/water interfaces," Langmuir **36**, 9368–9376 (2020).
[27]J. Noh, Y. Wang, H.-L. Liang, V. S. R. Jampani, A. Majumdar, and J. P. F. Lagerwall, "Dynamic tuning of the director field in liquid crystal shells using block copolymers," Phys. Rev. Res. **2**, 033160 (2020).
[28]D. Sec, T. Lopez-Leon, M. Nobili, C. Blanc, A. Fernandez-Nieves, M. Ravnik, and S. Zumer, "Defect trajectories in nematic shells: Role of elastic anisotropy and thickness heterogeneity," Phys. Rev. E **86**, 020705(R) (2012).
[29]H.-L. Liang, S. Schymura, P. Rudquist, and J. Lagerwall, "Nematic-smectic transition under confinement in liquid crystalline colloidal shells," Phys. Rev. Lett. **106**, 247801 (2011).
[30]T. Lopez-Leon, A. Fernandez-Nieves, M. Nobili, and C. Blanc, "Nematic-smectic transition in spherical shells," Phys. Rev. Lett. **106**, 247802 (2011).
[31]J. Noh, B. Henx, and J. P. Lagerwall, "Taming liquid crystal self-assembly: The multifaceted response of nematic and smectic shells to polymerization," Adv. Mater. **28**, 10170–10174 (2016).
[32]D. Thomsen, P. Keller, J. Naciri, R. Pink, H. Jeon, D. Shenoy, and B. Ratna, "Liquid crystal elastomers with mechanical properties of a muscle," Macromolecules **34**, 5868–5875 (2001).

[33]Y. Geng, R. Kizhakidathazhath, and J. P. Lagerwall, "Encoding hidden information onto surfaces using polymerized cholesteric spherical reflectors," Adv. Funct. Mater. **31**, 2100399 (2021).
[34]D. Broer, G. Crawford, and S. Zumer, *Cross-Linked Liquid Crystalline Systems: From Rigid Polymer Networks to Elastomers*, Liquid Crystals Book Series (CRC Press, 2011).
[35]I. Kundler and H. Finkelmann, "Strain-induced director reorientation in nematic liquid single crystal elastomers," Macromol. Rapid Commun. **16**, 679–686 (1995).
[36]I. Kundler and H. Finkelmann, "Director reorientation via stripe-domains in nematic elastomers: Influence of cross-link density, anisotropy of the network and smectic clusters," Macromol. Chem. Phys. **199**, 677–686 (1998).
[37]G. Verwey, M. Warner, and E. Terentjev, "Elastic instability and stripe domains in liquid crystalline elastomers," J. Phys. II **6**, 1273–1290 (1996).
[38]A. S. Utada, E. Lorenceau, D. R. Link, P. D. Kaplan, H. A. Stone, and D. A. Weitz, "Monodisperse double emulsions generated from a microcapillary device," Science **308**, 537–541 (2005).